Molecular Analysis of Murine Kit^{K641E} Melanoma Progression

Emily Everdell[1,2,3], Zhenyu Ji[1,2,3], Ching-Ni Njauw[1,2] and Hensin Tsao[1,2]

Acral and mucosal melanomas are often driven by sequence variants in the KIT receptor tyrosine kinase, with nearly 40% harboring alterations in the *KIT* locus. Despite advances in the knowledge of *KIT*-mutated melanomas, little is known about the molecular reprogramming that occurs during KIT-mediated melanoma progression owing to the rarity of acral and mucosal melanomas and the lack of comprehensive biological tools and models. To this end, we used a murine model that allows us to ascertain the molecular underpinnings of the stages of cancer progression—transformation, tumorigenesis, immune engagement, and tumor escalation. We found dramatic increases in biosynthetic demands associated with the transformation stage, including DNA and RNA metabolism, leading to replication stress. Tumorigenesis was closely linked to neuronal and axonal development, likely necessary for invasion into the host. Immune engagement highlighted early immune excitation and rejection pathways, possibly triggered by abrupt neoantigen exposure. Finally, tumor escalation pathways proved consistent with immune evasion, with immune-related pathways becoming significantly downregulated. To our knowledge, it is previously unreported that these critical milestones needed for KIT-driven melanoma tumor formation have been studied at the molecular level using isogenically matched and phenotypically defined cells.

Keywords: KIT, Melanoma, Molecular analysis, Murine cellular model

INTRODUCTION

Acral and mucosal melanomas, although less common, are more deadly than other types of melanoma. Acral lentiginous melanomas (ALMs) primarily occur on the palms, soles, and nailbeds, accounting for only 2−3% of all cutaneous malignant melanomas (Bradford et al, 2009). Among different racial groups, ALM is the most prevalent melanoma type among African Americans (Reintgen et al, 1982) and Asians (Kong et al, 2011). Unfortunately, ALMs are often diagnosed at a more advanced stage, with only 41% detected early (ie, <1.00 mm) and 37% discovered after the tumor exceeds 2.00 mm, resulting in lower 5- and 10-year survival rates of 80.3 and 67.5%, respectively. In contrast, common forms of melanoma have higher survival rates of 91.3 and 87.5% at 5 and 10 years, respectively (Bradford et al, 2009). A recent analysis of the SEER (Surveillance, Epidemiology, and End Results) database reveals concerning trends. From 1989 to 2009, the thickness of ALM significantly increased by 3.1% every 3 years, whereas common melanomas, such as superficial spreading melanoma, decreased by 1.0% every 3 years (Shaikh et al, 2015). This trend has led to a decrease in mortality among Whites but not among Blacks or Asian/Pacific Islanders (Shaikh et al, 2015). These findings support previous reports indicating a significant survival disparity among minorities compared with that among Whites (Rouhani et al, 2008; Wu et al, 2011; Zell et al, 2008). Mucosal melanomas, accounting for only 1.4% of all melanomas (Mihajlovic et al, 2012), also exhibit a poor prognosis with an expected 5-year survival rate of only 25% (Chang et al, 1998). Acral lentiginous and mucosal melanomas make up <5% of all melanomas but carry a significantly worse prognosis.

Acral and mucosal melanomas are genetically distinct from common melanomas and are more often associated with the *KIT* receptor tyrosine kinase. Research has shown that approximately 20−40% of acral melanomas harbor alterations, including amplifications and missense variants, in the *KIT* locus, although sequence variants in *BRAF* and *NRAS* also occur in ALM (Beadling et al, 2008; Curtin et al, 2005; de Lima Vazquez et al, 2016; Zebary et al, 2013). Mucosal melanomas exhibit sequence variants in *NRAS*, *BRAF*, and *KIT* in approximately 18, 16, and 15% of cases, respectively (Newell et al, 2019).

KIT sequence variants are predominantly missense variants scattered across the coding region, with 4 recurrent variants considered hotspot lesions in various cancer types (K642E, V559A, L576P, and W557R) (Meng and Carvajal, 2019). Among these, the *KIT*^{K642E} variant in the tyrosine kinase domain is the most prevalent in melanoma. Similar to other cancer-related receptor tyrosine kinases, oncogenic *KIT*

[1]Wellman Center for Photomedicine, Massachusetts General Hospital, Harvard Medical School, Boston, Massachusetts, USA; and [2]Department of Dermatology, Massachusetts General Hospital, Harvard Medical School, Boston, Massachusetts, USA

[3]These authors contributed equally to this work.

Correspondence: Hensin Tsao, Wellman Center for Photomedicine, Massachusetts General Hospital, Edwards 211, 50 Blossom Street, Boston, Massachusetts 02466, USA. E-mail: htsao@mgh.harvard.edu

Cite this article as: JID Innovations 2024;4:100266

variants activate downstream signaling pathways such as RAF/extracellular signal–regulated kinase and phosphoinositide 3-kinase/protein kinase B, contributing to tumor growth and survival (Todd et al, 2013; Zhan et al, 2017).

However, despite the knowledge about *KIT* variants, there are gaps in understanding the process of KIT-driven melanomagenesis owing to the rarity of ALMs and the lack of comprehensive biological tools and models. Notably, genetically engineered mouse models with activated Kit^{K641E} have been developed, but they primarily develop gastrointestinal tumors and not melanomas (Rubin et al, 2005). To bridge this gap and enhance our understanding of KIT-driven melanomagenesis in acral and mucosal melanomas, a murine Kit^{K641E} cellular model was recently developed (Njauw et al, 2022) that recapitulates the various stages of cancer progression: transformation, tumorigenesis, immune engagement, and tumor escalation (Figure 1). These Kit^{K641E} avatars afford a unique opportunity to understand the sequential molecular reprogramming required of all nascent cancer cells to negotiate the rites of oncogenic passage.

RESULTS

Overview of transcriptomic changes

The multistage mKit^{K641E} model (Njauw et al, 2022), the study's overall design, and the individual elements are outlined and annotated in Figure 1. Two approaches, individual stage-specific and global hierarchical clustering, were performed to better understand the molecular reprogramming associated with murine Kit^{K641E} tumor progression. Finally, pathways enriched from differentially expressed murine genes were compared with pathways correlated with *KIT*-variant status in human melanomas using The Cancer Genome Atlas SKCM cohort.

Principal component analysis (Figure 2a) was first performed to audit transcriptomic relationships, which revealed that the most significant molecular transition occurred during the initial transformation. The mKit^{K641E} lines were found to be more closely related to each other than to the untransformed vector cells. Interestingly, although the C1 and C3 cells were tumorigenic in C57BL/6 mice, the C3 cells appeared closer to the pretumorigenic (PT) cells in the expression space than the C1 cells. However, caution must be exercised in interpreting the precise distances from the principal components analysis given the limited number of samples and replicates. During the transformation process (Figure 2b and Supplementary Table S1), 10.2% of the differentially expressed genes were significantly upregulated by >2-fold (ie, +2FC*), whereas 10.7% of the differentially expressed genes were significantly reduced by >2-fold (ie, −2FC*). In contrast, during tumorigenesis in NSG mice (ie, PT to N1 cells) (Figure 2b and Supplementary Table S1), only 4.2 and 4.1% of the genes exhibited +2FC* and −2FC* changes, respectively. Only 3.9 and 3.1% of the transcriptome underwent significant expression shifts during immune engagement (Figure 2b and Supplementary Table S1) and tumor escalation (Figure 2b and Supplementary Table S1), respectively. These results suggest that the oncogenic switch triggered by Kit^{K641E} and the first introduction to the host microenvironment are the 2 most dramatic exposures for the aspiring cancer cell. To gain a better understanding of the molecular physiology underlying each phenotypic phase, we subjected the stage-specific differentially expressed genes to over-representation analysis (ORA) with gene ontology biological process (GOBP) terms and Gene Set Enrichment Analysis using Kyoto Encyclopedia of Genes and Genomes (KEGG), Panther, Reactome, and Wikipathway databases.

Stage-specific differential gene expression analysis

Transformation in vitro. After undergoing the initial Kit^{K641E} transformation, 21.0% of the transcriptome displayed significant alterations, resulting in substantial changes in the expression of gene sets associated with various cellular processes. There was general agreement between the GOBP syntaxes and pathway analyses (Figure 3a and Supplementary Table S2). These elements could be broadly assigned into several functional groupings, including cell cycle/mitosis, mitotic apparatus, nucleotide metabolism, DNA synthesis/replication, DNA repair/recombination, RNA processing/metabolism, ribosome biogenesis, amino acid metabolism, and cholesterol/lipid metabolism (Figure 3a and b). The dramatic programmatic changes indicate that transformation prepares the cell for increased substrate needs and metabolic demands associated with heightened cellular division.

Tumorigenesis in NSG mice. With the introduction of the Kit^{K641E}-transformed cells into an immunocompromised host,
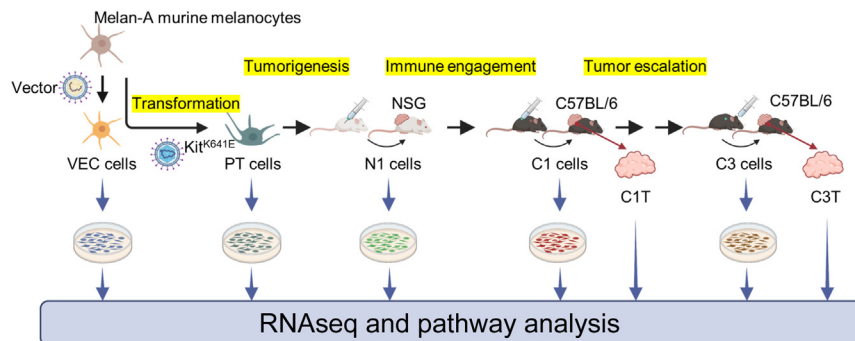

Figure 1. Multistage Kit^{K641E} model and analytical scheme. Per the manuscript by Njauw et al (2022), cells that were transformed phenotypically but had not been subjected to in vivo tumorigenesis assays were designated PT cells. Melanoma cells isolated and cultivated from the first NSG tumors were called N1 cells. N1 cells were then engrafted into C57BL/6 mice to produce first-generation C57BL/6 tumors (C1T and C1 cells). Subsequent passaging of C1 cells into further second and third generations of C57BL/6 passaging were designated C2 and C3, respectively. RNAseq, RNA sequencing; PT, pretumorigenic; VEC, vector.
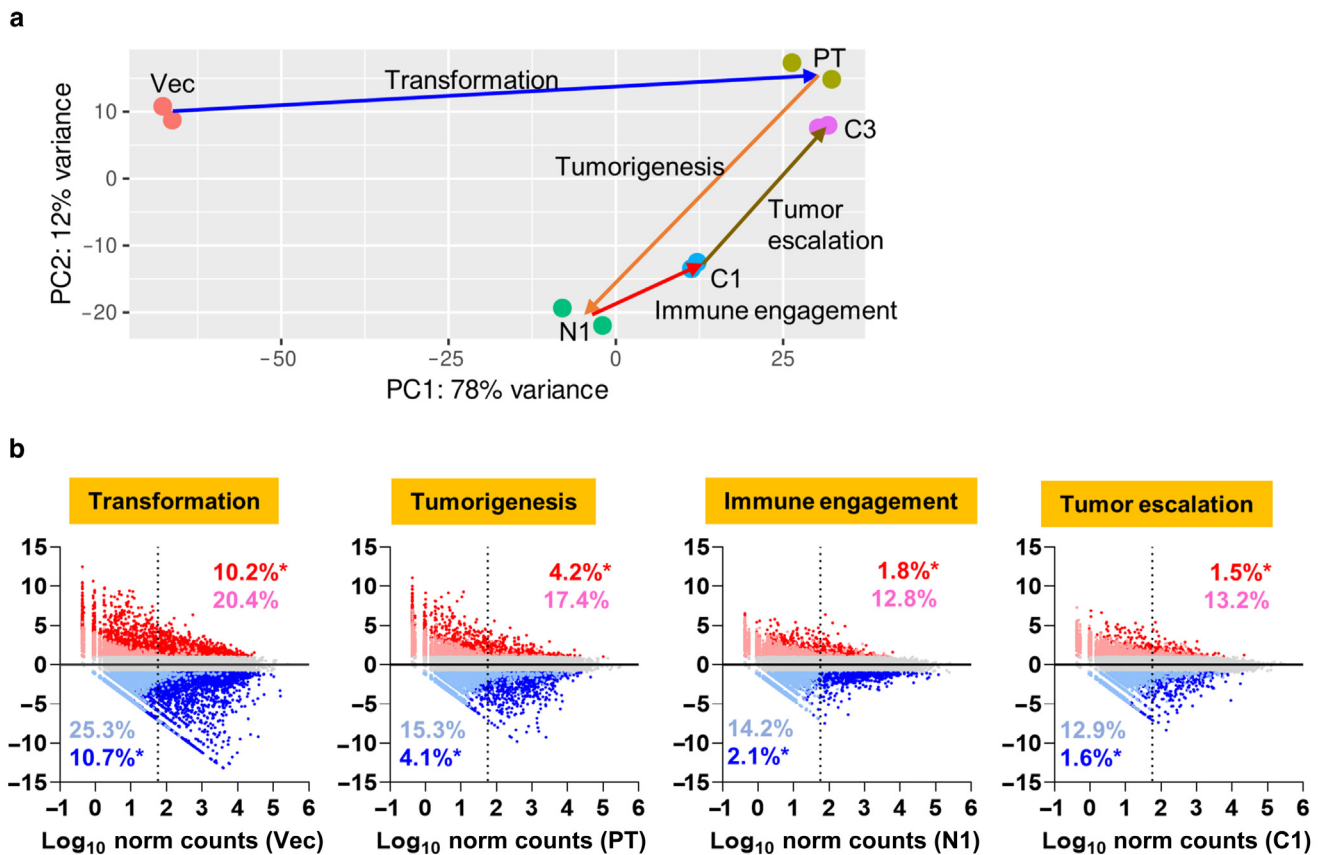
Figure 2. Global changes in expression. (**a**) PCA of RNAseq data from duplicate samples at each stage (left panel) and matrix of distances from PCA (right panel). (**b**) Global changes in gene expression at each stage. Each dot represents a single gene; red dots (both light red and dark red) and blue dots (both light blue and dark blue) represent genes that exhibit >2-fold increases (+2FC, text) and decreases (−2FC, text), respectively. Dark red and dark blue dots are those genes that also show a P_{adj} < .05 as determined by DESeq2. Numbers with the asterisk indicate the percentage of the genes that have been altered by >2-fold and P_{adj} < 0.05 (dark red dots = >2-fold increase, P_{adj} < .05, +2FC* in text; dark blue dots = >2-fold decrease, P_{adj} < .05, −2FC* in text). All data are shown in Supplementary Table S1. P_{adj}, adjusted *P*-value; PC, principal component; PCA, principal component analysis; RNASeq, RNA sequencing; VEC, vector.

a very different set of molecular programs emerged (Figure 3c and d and Supplementary Table S3). Tumorigenic biology appears to be closely linked to axon guidance/neural development (GOBP: synapse organization, q = 1.55E-07; KEGG: axon guidance, q = 5.28E-05), extracellular matrix, adhesion and motility, wound healing/angiogenesis, morphogenesis, and hemostasis. There were 52 genes within the synapse organization gene set that were significantly upregulated between the PT and N1 cells, including *Wnt5a* (log₂ fold change = +9.62), *Lingo2* (log₂ fold change = +9.08), and *Ctnnd2* (log₂ fold change = +6.63). Finally, several immune (ie, GOBP: response to IFNβ, q < 2.2E-16; IL-6 production, q = 4.00E-03) and virus-related (ie, KEGG: human papillomavirus infection, q = 1.53E-03; measles, q = 6.52E-03; influenza A, q = 0.041) gene ontology terms and pathways also exhibited enrichments.

Immune engagement in C57BL/6 mice. Surprisingly, immune engagement was associated with only minimal transcriptomic changes: 1.8 and 2.1% of the genes experienced significant +2FC* and −2FC* changes, respectively. Although gene ontology mapping did not reveal any significantly associated terms, pathway interrogation (Figure 3e and Supplementary Table S4) identified upregulation of immunogenicity (eg, KEGG: allograft rejection, normalized

enrichment score [NES] = +2.08, q = 2.37E-03; KEGG: antigen processing and presentation, NES = +2.03, q = 2.37E-03; KEGG: graft vs host, NES = +2.02, q = 1.58E-03), autoimmunity (eg, KEGG: autoimmune thyroid disease, NES = +2.00, q = 1.48E-03; KEGG: systemic lupus erythematosus, NES = +1.82, q = 1.16E-02), and infection (eg, KEGG: tuberculosis, NES = +1.79, q = 1.18E-02). Immune cell contamination is unlikely to account for the strong association between the immune molecular phenotype because C1 melanoma cells were subjected to short-term culture conditions to purge immune cells. These pathways point to a rejection program triggered by the mKit^K641E cells' initial contact with the immune system.

Tumor escalation. Similar to immune engagement, tumor escalation is associated with modest expression shifts of 1.5% +2FC* and 1.6% −2FC*. However, many immune rejection pathways that were positively associated with immune engagement became negatively correlated with tumor escalation (Figure 3f and Supplementary Table S5). Among KEGG pathways, allograft rejection, asthma, systemic lupus erythematosus, and autoimmune thyroid gene sets were significantly upregulated during immune engagement but subsequently downregulated during tumor escalation (Figure 3g).
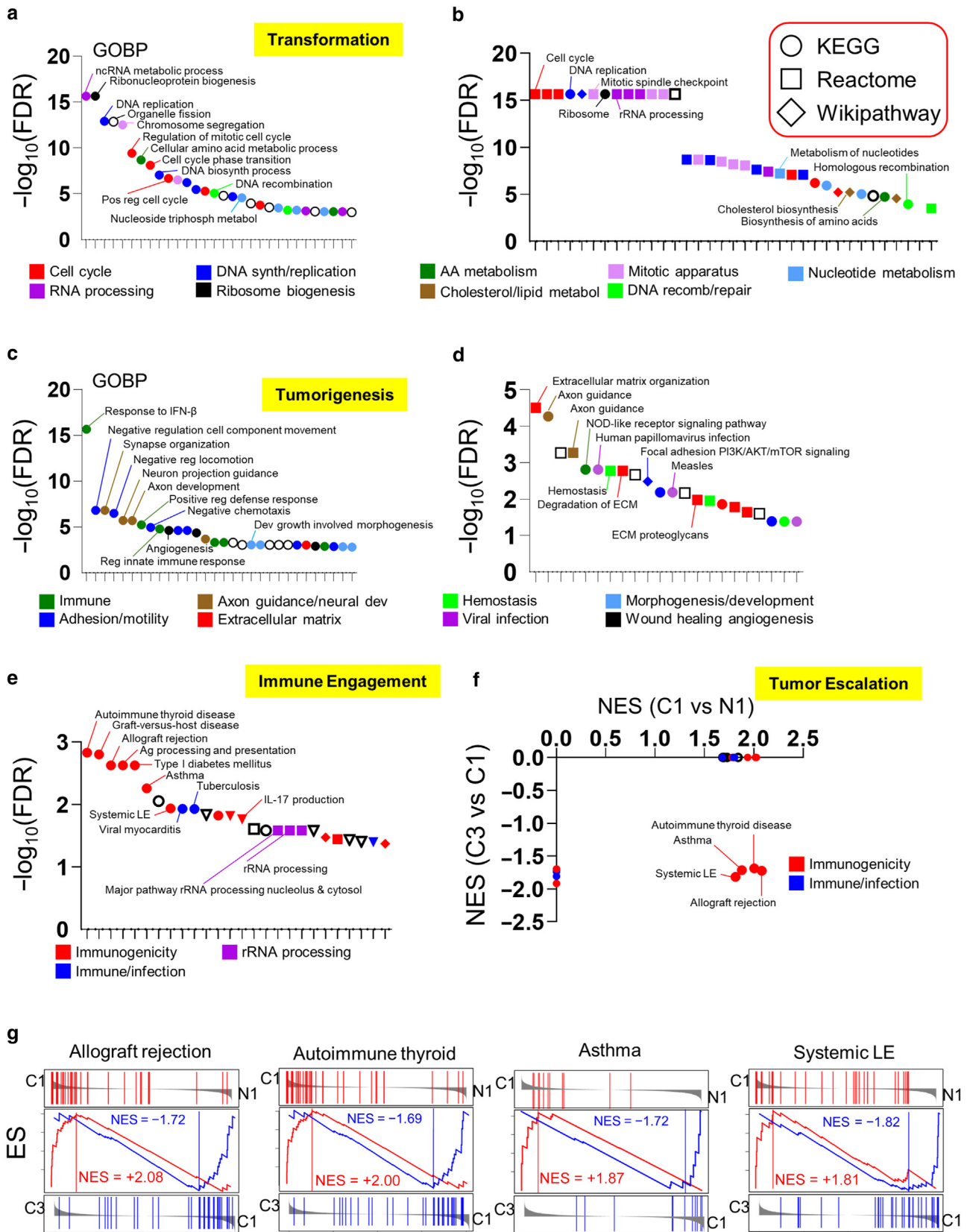
Figure 3. Stage-wise pathway analysis. Pathway analysis using the online Webgestalt package (https://www.webgestalt.org/). Default parameters used were (i) minimum number of IDs in the category: 5; (ii) maximum number of IDs in the category: 20000; (iii) significance level: FDR < 0.05; number of permutation: 1000. −log10FDR was used to accommodate statistical significance for both GSEA and ORA. Gene ontology-biological processes (GOBP) during transformation **(a)** and tumorigenesis **(c)** as determined by ORA. Pathway analyses for **(b)** transformation and **(d)** tumorigenesis as determined by GSEA. Functional groupings were manually curated and color coded as indicated in the figure. **(e)** Pathway analysis of immune engagement by GSEA. **(f)** Directionality of significant

Tumor tissues available from C1 and C3 xenografts were then subjected to RNA sequencing. Comparison of the C3 and C1 tumor gene expression profiles (C3T vs C1T) (Supplementary Table S6) confirmed the suppression (ie, negative NES) (Figure 4a) of immune-related pathways (red symbols) (Figure 4a) (eg, KEGG: allograft rejection, NES = −2.18, q < 2.2E-16; KEGG: autoimmune thyroid disease, NES = −2.15, q < 2.2E-16; KEGG: graft vs host, NES = −2.14, q < 2.2E-16). Transcriptome-based immune infiltrate analysis (Sturm et al, 2019) showed reduced CD8+ in C3T compared with that in C1T (Figure 4b) (red box). C3T also exhibited activation of the same replication and biosynthetic pathways seen with initial transformation (Supplementary Table S6) (eg, KEGG: DNA replication, NES = +2.18, q = 1.86E-03; cell cycle, NES = +2.15, q = 2.79E-03; ribosome biogenesis in eukaryotes, NES = +1.94, q = 0.01). Thus, tumor escalation from C1T to C3T encompasses an acceleration of the proliferative apparatus and an evasion of immune surveillance.

Clustering by expression trend

Because the various mKit^{K641E} lines were derived from sequential manipulation, we next undertook a different strategy to probe for pathway relationships among the classes. Using all genes that exhibited a significant change across the stages identified by the likelihood ratio test, we subjected 9973 genes to degPatterns analysis. As shown in Figure 5a, this yielded 22 clusters (ie, clusters 1−22) (Supplementary Table S7) with varying trends of expression progressing from vector to C3. Using the mean expression values of each cluster at the various stages, we further collapsed these clusters into 7 superclusters (Figure 5a) (upper panels I−VII). Normalized trends (to vector) are shown in Figure 5b (lower panel), with the various clusters colored coded within their superclusters.

Because genes in each cluster were only enumerated and not ranked by expression, we performed ORA on each cluster by independently mapping cluster-specific genes to KEGG, Panther, Reactome, and Wikipathway databases (Figure 6 and Supplementary Table S7). Clusters 3, 8, 15, 17, and 20 comprise supercluster I (Figure 6a), which was the largest supercluster (n = 2460 genes) and was characterized by sustained elevations through all stages (c3, c8, c15, c17, c20 mean normalized clusters ($\overline{CL}_{norm}$), PT: $\overline{CL}_{norm}$ = +1.07; N1: $\overline{CL}_{norm}$ = +1.09; C1: $\overline{CL}_{norm}$ = +1.09; C3: $\overline{CL}_{norm}$ = +1.07). Cluster 3, which had the most elements (n = 1339) also showed the greatest number of significant enrichments (n = 155 pathways, q < 0.05). The strongest associations (q < 2.20E-16) functionally coalesced around cell cycle/mitosis (amplification of signal from the kinetochores, R = 5.91, q < 2.20E-16; cell cycle, R = 3.34, q < 2.20E-16; cell cycle checkpoints, R = 4.82, q < 2.20E-16; cell cycle, mitotic, R = 3.33, q < 2.20E-16; G2/M checkpoints, R = 4.42, q < 2.20E-

16; M phase, R = 2.98, q < 2.20E-16), DNA replication/repair/synthesis (DNA repair, R = 3.12, q < 2.20E-16; DNA replication, R = 4.72, q < 2.20E-16; synthesis of DNA, R = 4.69, q < 2.20E-16), and RNA metabolism (major pathway of ribosomal RNA processing in the nucleolus and cytosol, R = 7.50, q < 2.20E-16; metabolism of RNA, R = 3.86, q < 2.20E-16; RNA transport, R = 4.14, q < 2.20E-16; ribosomal RNA processing, R = 7.50, q < 2.20E-16; ribosomal RNA processing in the nucleus and cytosol, R = 7.50, q < 2.20E-16). Although c8 (n = 449 genes; n = 133 pathways, q < 0.05) shared cell cycle/mitosis and DNA replication/repair/synthesis pathways similar to those of c3, c8 appeared to be selectively enriched for the hedgehog pathways compared with all other clusters (degradation of Gli1 by the proteasome, R = 6.66, q = 1.45E-04; Gli3 is processed to Gli3R by the proteasome, R = 6.4243, q = 1.87E-04; hedgehog ligand biogenesis, R = 6.00, q = 3.24E-04; hedgehog off state, R = 4.53, q = 2.56E-04; hedgehog on state, R = 4.75, q = 1.62E-04; signaling by hedgehog, R = 3.74, q = 7.01E-04). Between c3 and c8, there were 15 pathways involving p53, including transcriptional regulation by p53 (R = 2.60, q = 3.76E-09) and regulation of p53 activity through phosphorylation (R = 3.83, q = 3.96E-08). Clusters c15 (n = 315 genes, n = 12 pathways, q < 0.05), c17 (n = 192 genes, n = 9 pathways, q < 0.05), and c20 (n = 165 genes, n = 1 pathway, q < 0.05) did not harbor any distinct pathway enrichments.

Clusters 5 and 10 (supercluster II) showed similar contours with a rapid decrease in gene expression upon initial transformation (PT) and subsequent recovery during tumorigenesis (N1). Cluster 5 (Figure 6b) (n = 1423 genes, n = 68 pathways, q < 0.05) was the largest cluster within supercluster II; c10 had only n = 129 genes and demonstrated no significant enrichments. Although c5 did harbor some extracellular matrix/motility pathways, there were multiple hits related to immune physiology (NOD-like receptor signaling pathway, R = 3.04, q = 6.02E-06; IL-2 signaling pathway, R = 3.29, q = 8.06E-04; immune system, R = 1.40, q = 1.22E-03; IL-7 signaling pathway, R = 4.01, q = 1.41E-03; IL-3 signaling pathway, R = 2.80, q = 1.45E-03; IL-9 signaling pathway, R = 4.90, q = 3.97E-03), which were uniquely restricted to c5.

Supercluster III showed mixed pathway correlations, with c2 exhibiting the most extensive enrichments (Figure 6c) (n = 991 genes, n = 40 pathways, q < 0.05). Although supercluster III genes, in general, diminished in expression after transformation, c2 genes did modestly recover expression with tumorigenesis (Figure 5a), which could account for the multiple pathways linked to extracellular matrix and motility (Figure 6c) similar to the stage-wise analysis for tumorigenesis (Figure 3c).

In supercluster IV (Figure 5a) (c1, c4, c11, and c22) relative gene expression (to vector) increased during transformation,
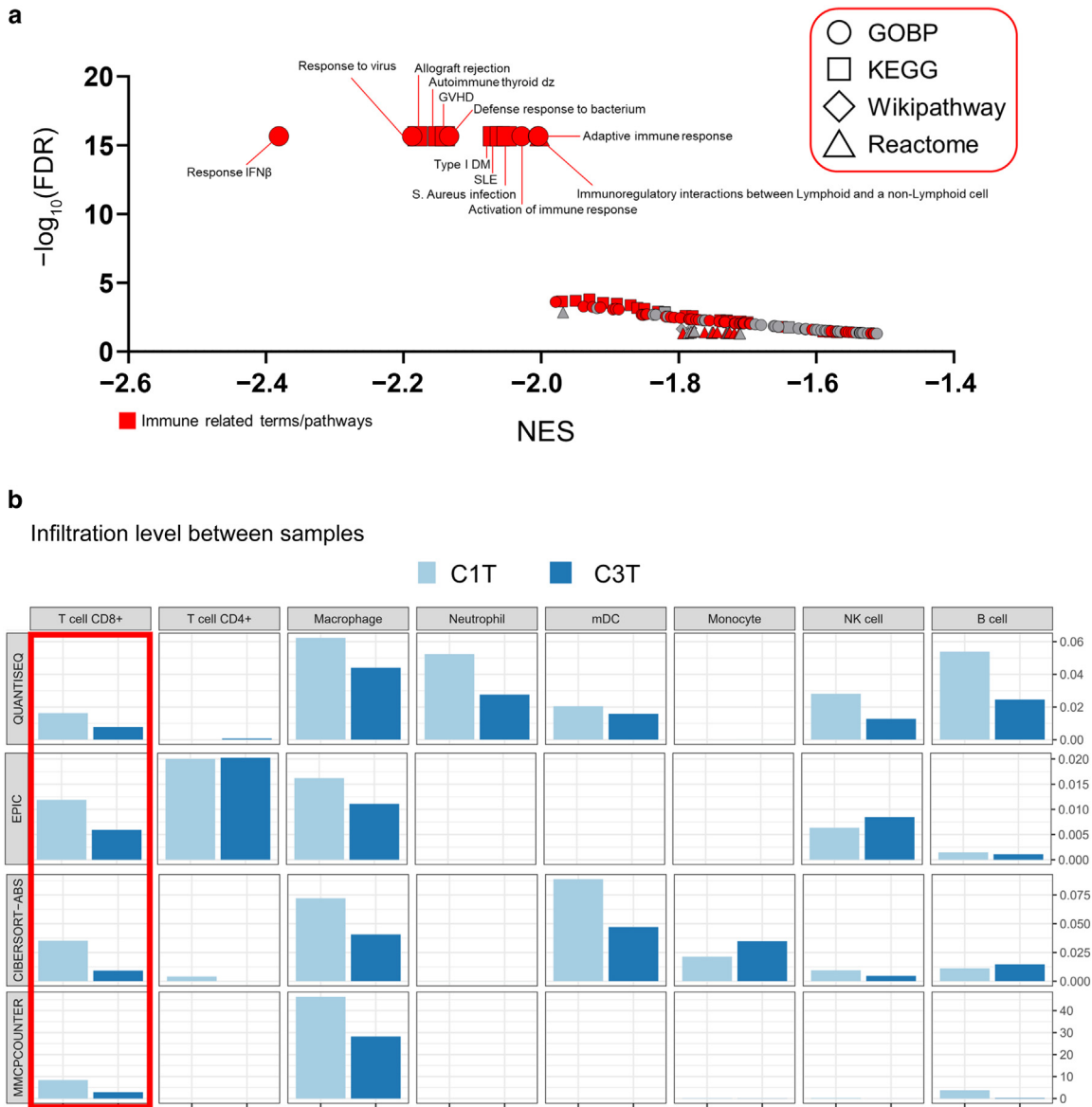
Figure 4. Pathway and tumor infiltrate analysis of C3T versus C1T. (**a**) RNAseq data for C1T and C3T tumors were subjected to GSEA analysis using parameters outlined in the Materials and Methods. Symbol shapes indicate pathways identified, whereas red color symbols represent pathways related to immunity. The negative NES indicates a decrease in the expression of genes mapped to those pathways as tumor progressed from C1T to C3T. (**b**) Cellular profiling of tumor immune infiltrates from bulk RNAseq showing a consistent decrease in CD8+ cells from C1T to C3T, in consonant with ongoing immune escape during tumor escalation. All data are shown in Supplementary Table S6. FDR, false discovery rate; GOBP, gene ontology Biological process; GSEA, gene set enrichment analysis; GVHD, graft vs host disease; KEGG, Kyoto Encyclopedia of Genes and Genomes; RNAseq, RNA sequencing.

peaked with the PT cells ($\overline{CL}_{norm} = +1.13$), and subsequently declined at the N1 stage modestly ($\overline{CL}_{norm} = +1.05$) but remained elevated at c1 and c3. c1 transcripts (Figure 6d) (n = 1060, n = 22 pathways, q < 0.05) were significantly enriched (q < 0.05) in 22 significant pathways, with most of these functionally organizing around ribosome and translation (Figure 6d) (eg, ribosome, R = 7.22, q < 2.20E-16; cytoplasmic ribosomal proteins, R = 8.89, q < 2.20E-16; CAP-dependent translation initiation, R = 8.50, q < 2.20E-16; eukaryotic translation initiation, R = 8.50, q < 2.20E-16). On the other hand, c4 (n = 306; 14 pathways, q < 0.05) genes almost exclusively coalesced around cholesterol and steroid metabolism pathways (Figure 6d) (eg, cholesterol biosynthesis, R = 49.29, q = 1.23E-13; metabolism of

steroids, R = 6.313, q = 8.37E-05). c11 demonstrated 2 weak associations (fatty acid biosynthesis, R = 7.03, q = 0.025; eicosanoid synthesis, R = 7.17; q = 0.043), whereas c22 had none. Superclusters V–VII (c9, c13, c14, c16, c18, c19, and c21) had very few associated pathways, given the limited number of genetic elements within each cluster (Supplementary Table S7).

Comparison between human and mouse *Kit*-mutated programs
Next, we determined whether any of the molecular programs predominating the murine Kit^{K641E} cells were associated with *Kit* variants in human melanomas. For human melanomas, we interrogated The Cancer Genome Atlas SKCM tumors
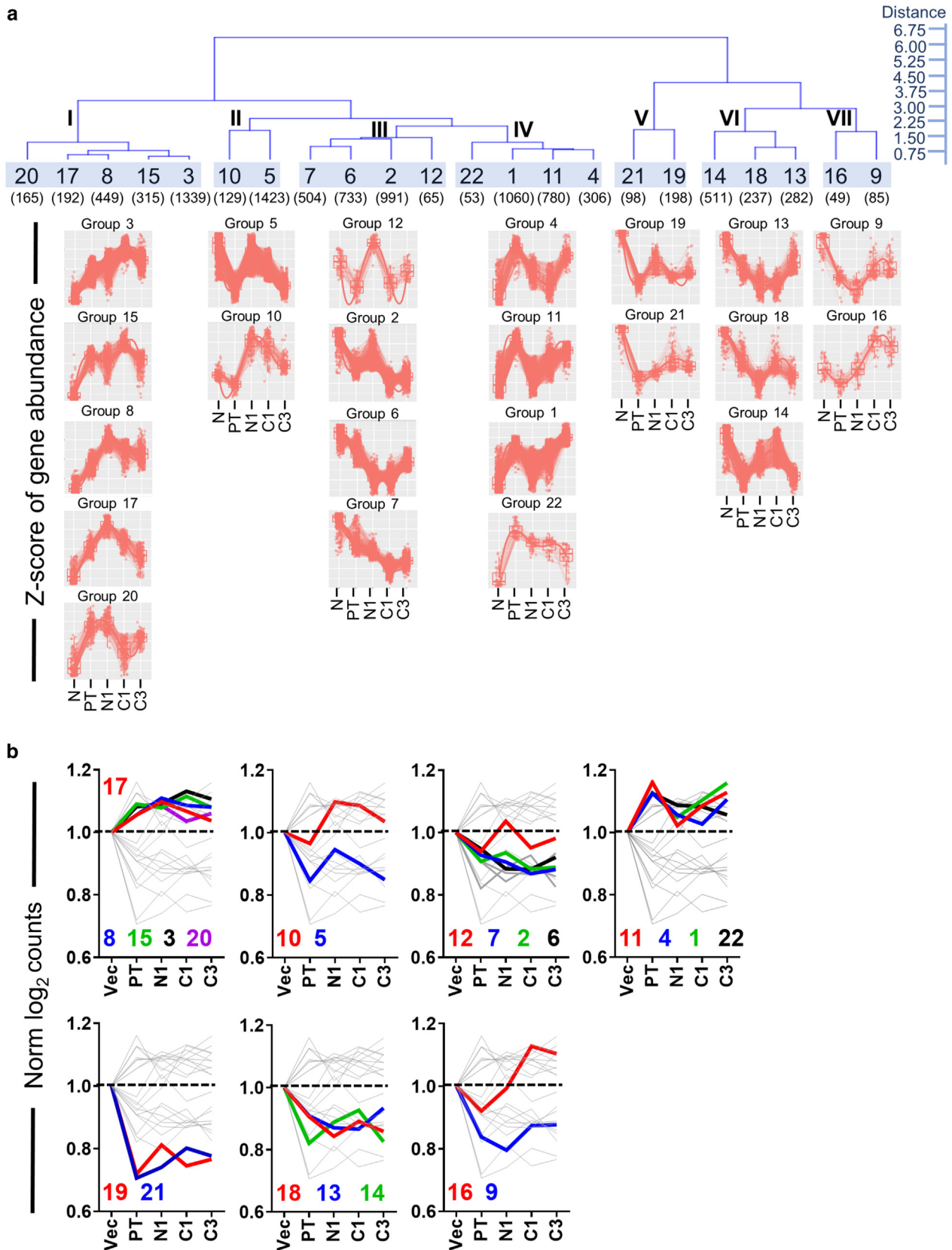
Figure 5. Clustering by gene expression trends. (a) Upper panel: superclusters (I–VII) generated by hierarchical clustering of mean expression values in each cluster (c1–c22) by stage. The number of gene elements within each cluster is shown in parentheses. Below each supercluster, the actual expression profiles (normalized to Z-score of gene abundance within each sample—N, PT, N1, C1, C3) for each gene assigned to each cluster are shown. (b) Composite representation with each cluster's relative (vector = 1) expression contour in color coding. All data are shown in Supplementary Table S7. PT, pretumorigenic; Vec, vector.
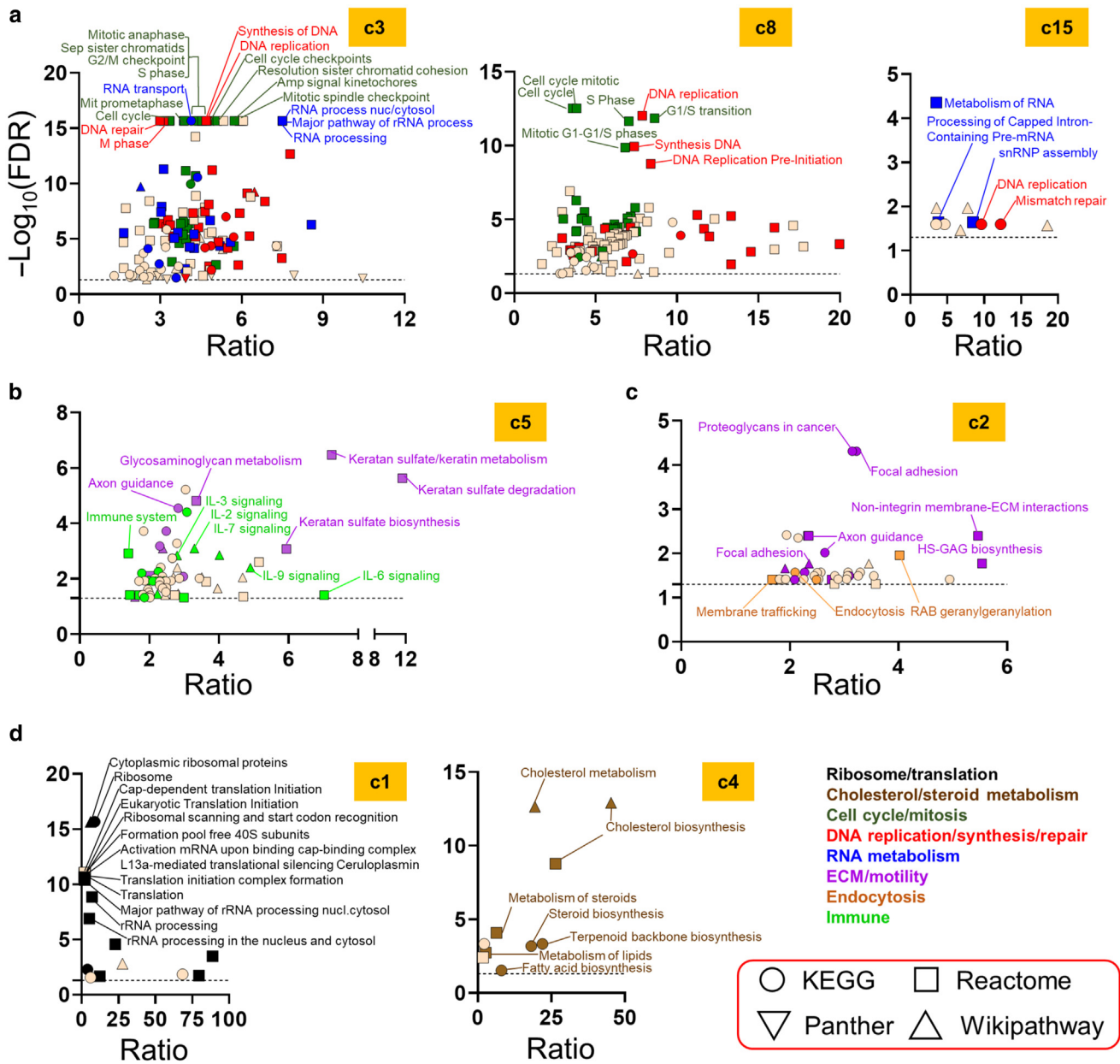
Figure 6. Pathway analysis of individual expression clusters. Over-representation analyses of selected clusters with the highest number of significantly associated pathways (KEGG, circle; Reactome, square; Wikipathway, up triangle; and Panther, down triangle). Clusters **(a)** c3, c8, and c15 from supercluster I; **(b)** c5 from supercluster II; **(c)** c2 from supercluster III; and **(d)** c1 and c4 from supercluster IV are shown. Ratios represent the number of observed genes divided by the expected value. Selected dominant pathways are expressed as functional groupings, which were manually curated and color coded. All data are presented in Supplementary Table S7. FDR, false discovery rate; KEGG, Kyoto Encyclopedia of Genes and Genomes.

(n = 363) using the PanCancer sample set and identified 42 human samples (12%) with *Kit* alterations (sequence variants, copy number amplifications, and amplified expression, h*KIT*[alt]) (Supplementary Table S8). Comparison between KIT-altered and unaltered human melanomas revealed 885 genes (Supplementary Table S9) that were preferentially expressed in the *KIT*-altered samples over *KIT*-unaltered samples ($\log_2$ fold change > 0, *P* < .05) (Figure 7a, left panel, red dots), thus defining a nominal h*KIT*[alt] signature. To examine KIT-selective changes and model human *KIT*-mutant melanomas more closely, we defined the murine Kit[K641E] signature as genes overexpressed in C3 cells (Kit[K641E]) versus vector

(Kit[WT]) ($\log_2$ fold change > 0, adjusted *P* < .05) (Figure 7a, right panel, blue dots), which yielded 4060 genes (Supplementary Table S10). Although all *KIT* sequence variants in h*KIT*[alt] samples may not necessarily activate c-Kit, there were too few h*KIT*[K642E] alterations alone for meaningful comparison.

We first undertook a gene-by-gene comparison. The distinct gene spaces for murine (n = 23,719) and human (n = 19,652) transcriptomes were parsed into a minimal set of n = 13,453 orthologs with identical gene symbols. From this group, 237 genes were common to both mKit[K641E] and h*KIT*[alt] signatures (mKit[K641E] ∩ h*KIT*[alt]) within the ortholog
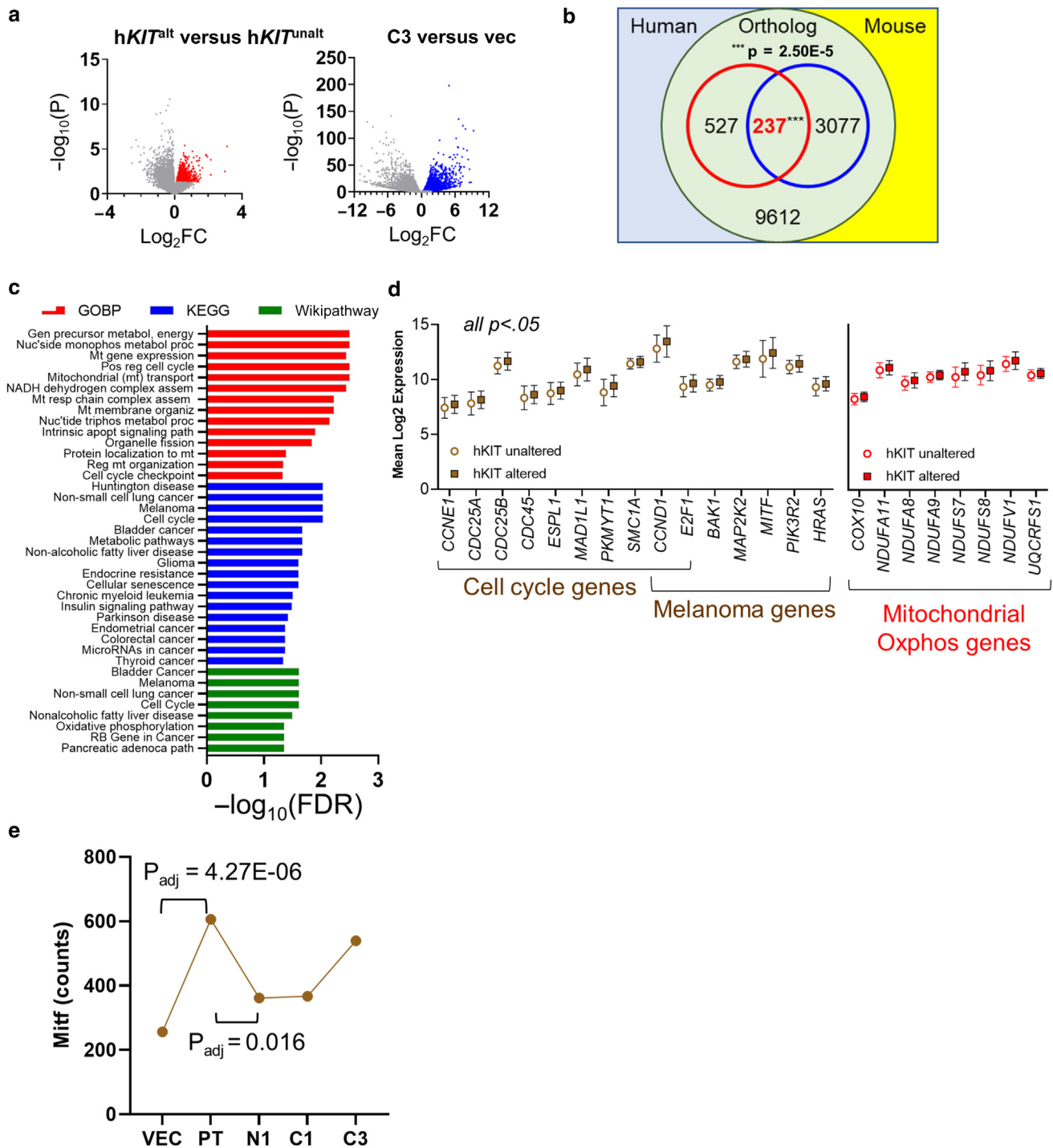
Figure 7. Overlap between mKit[K641E] and human *KIT*-altered melanomas in gene-by-gene comparison. (**a**) Left panel: volcano plot showing genes that are enriched in human *KIT*-altered melanoma tumors (human *KIT*[alt] signature: red dots, $\log_2FC > 0$, $P < .05$); Right panel: genes associated with murine kit* melanoma cells (murine Kit[K641E] signature: blue dots, $\log_2FC > 0$, $P < .05$. (**b**) An ortholog space (mouse ∩ human genes) was defined as 13,453 genes with identical gene designations between human and mouse. Within the ortholog space were n = 734 hKITalt signature genes and n = 3314 Kit[K641E] signature genes. n = 237 were shared between the h*KIT*[alt] genes and Kit[K641E] signature gene sets (*P* = 2.50E-05, chi-square). (**c**) Pathway mapping by over-representation analysis for the overlap gene set (n = 237). (**d**) Cell cycle, melanoma, and mitochondrial/oxphos genes were significantly elevated in human *KIT*[alt] tumors. (**e**) *Mitf* gene counts by Kit[K641E] stage. P_{adj} values comparing expression levels at each stage are derived from the DESeq2 program, which uses the Wald test and adjusts for multiple testing using the Benjamini and Hochberg methods. A statistically significant increase and decrease in *Mitf* levels can be observed at the initial Kit[K641E] transformation stage and the subsequent tumorigenesis stage, respectively. TCGA_SKCM tumors in the h*KIT*[alt] set are enumerated in Supplementary Table S8. All other expression analyses are presented in Supplementary Tables S9–11. FC, fold change; FDR, false discovery rate; P_{adj}, adjusted *P*-value; PT, pretumorigenic; TCGA, The Cancer Genome Atlas; VEC, vector.

space (chi-square = 17.8; P = 2.50E-05) (Figure 7b and Supplementary Table S11). These KIT-overlap genes were then subjected to ORA using GOBPs, KEGG, and Wikipathway databases (all false discovery rate < 0.05 in Supplementary Table S11). The top terms/pathways derived from the overlap set involved the cell cycle pathway (Figure 7c) (eg, KEGG cell cycle, q = 9.35E-03; GOBP-positive regulation of cell cycle, q = 3.17E-03; Wikipathway: cell cycle, q = 0.025) with the representative members shown in Figure 7d.

There was also upregulation of the melanoma gene set in both hKIT^{alt} and mKit^{K641E} tumors (Supplementary Table S11) (KEGG: Hsa05218/melanoma, q = 9.35E-03; Wikipathway: WP4685/melanoma, q = 0.025). *MITF*—a known biological target of c-Kit activation (Shibahara et al, 2001)—was more highly expressed in both murine and human *KIT*-mutated tumors (C3 vs vector: 2.1-fold, adjusted P = 1.48E-05; hKIT^{alt} vs hKIT^{unalt}: 1.5-fold, P = .026). To pinpoint the possible stage at which Kit^{K641E} regulates *Mitf*, we examined *Mitf* expression in the mKit^{K641E} model and found that initial transformation led to the highest and most significant induction of *Mitf* (Figure 7e) (log$_2$ fold change = +2.37, adjusted P = 4.27E-06, DESeq2), suggesting that upregulation occurs as a direct result of Kit^{K641E} transformation and not owing to microenvironmental or immune selection in the host. Further supportive evidence for a relationship between *KIT* and lineage programming in human melanomas comes from the consistent and significant positive correlations between *KIT* and pigmentation genes (Supplementary Table S12), including *MITF* (Spearman: 0.31, q = 2.77E-07), *SOX10* (Spearman: 0.26, q = 1.87E-05), *PAX3*

(Spearman: 0.20, q = 8.69E-04), *TYR* (Spearman: 0.28, q = 1.83E-06), *TYRP1* (Spearman: 0.31, q = 2.80E-07), and *MLANA* (Spearman: 0.31, q = 1.67E-07). Finally, there were also strong and shared enrichments for mitochondrial and cellular energetics terms/gene sets (Figure 7c and Supplementary Table S11) (eg, GOBP mitochondrial gene expression, q = 3.17E-03; GOBP, mitochondrial transport, q = 3.61E-03, Wikipathway oxidation phosphorylation, q = 0.045), including *COX10* and multiple *NDUF* genes (Figure 7d).

We then initiated a pathway-by-pathway comparison because functional orthologous groups could arise from related but distinct genes. The hKIT^{alt} (n = 885 genes) and mKit^{K641E} (n = 4060 genes) signatures were independently subjected to GOBP, KEGG, Reactome, and Wikipathway analyses and scrutinized for shared terms/pathways (Figure 8a). Supplementary Table S13 lists the nominally significant (P < .05) or top 100 most correlated pathways. The top GOBP terms and pathways associated with hKIT^{alt} genes were pigmentation (GOBP: q = 4.87E-03), endometrial cancer (KEGG: q = 5.53E-03), and 22q11.2 deletion syndrome (Wikipathway: q = 2.15E-03), whereas those enriched with the mKit^{K641E} genes included chromosome segregation (GOBP: q = 2.20E-16), DNA replication (GOBP: q = 2.20E-16), ribosome (KEGG: q = 2.20E-16), activation of ATR in response to replication stress (Reactome: q = 6.56E-15), cytoplasmic ribosomal protein (Wikipathway: q = 2.20E-16), and DNA replication (Wikipathway: q = 2.20E-16).

In descending order, the number of human/murine pathway overlaps was n = 24, n = 18, n = 7, and n = 3 for KEGG, GOBP, Reactome, and Wiki pathways, respectively
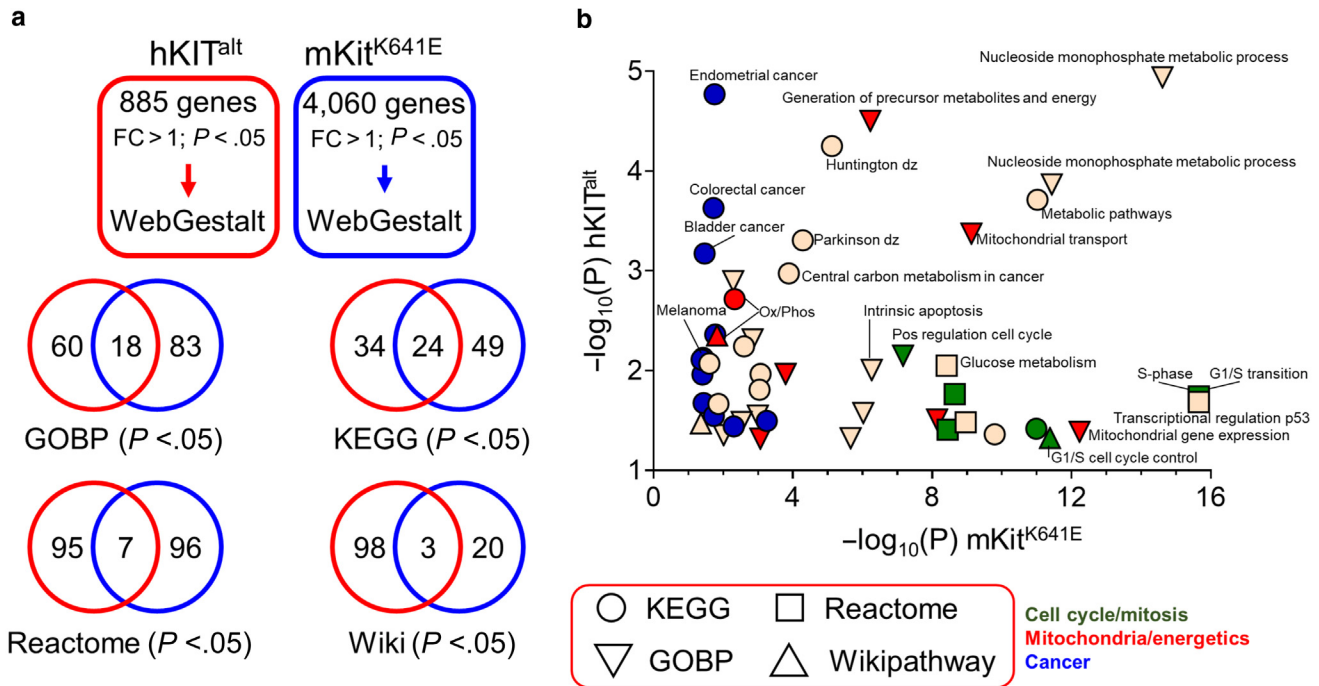

Figure 8. Pathway-by-pathway analysis between human *KIT*-altered and mouse Kit^{K641E} melanomas. (**a**) Human KIT^{alt} signature and murine Kit^{K641E} signature genes were independently subjected to gene ontology and pathway analyses using Webgestalt as described in the Materials and Methods. (**b**) Negative log$_{10}$-transformed P-values for common human KIT^{alt} and murine Kit^{K641E} pathways. All data are shown in Supplementary Table S13. FC, fold change; GOBP, gene ontology biological process; KEGG, Kyoto Encyclopedia of Genes and Genomes.

(Figure 8b). Significant KEGG sharing was observed with cancer (eg, endometrial cancer, P_{hKIT*} = 1.15E-05, P_{mKit*} = 1.79E-02; melanoma, P_{hKIT*} = 7.75E-03, P_{mKit*} = 4.20E-02), neurodegenerative disease (eg, Huntington's disease, P_{hKIT*} = 5.62E-05, P_{mKit*} = 7.56E-06; Parkinson's disease, P_{hKIT*} = 4.94E-04, P_{mKit*} = 5.20E-05), and oxidative phosphorylation (P_{hKIT*} = 1.92E-03, P_{mKit*} = 4.74E-03). Numerous pathways related to cell cycle and mitochondrial physiology/energetics also mapped to both h*KIT*^{alt} and Kit^{K641E} signatures (Figure 8b), consonant with the gene-by-gene findings (Figure 7c and d).

DISCUSSION

Hanahan and Weinberg (2011) proposed and updated the hallmarks of cancer in 2011, providing a framework for understanding the complexities of cancer. The 8 hallmarks include sustained proliferative signaling, evasion of growth suppressors, resistance to cell death, replicative immortality, angiogenesis, invasion and metastasis, metabolic reprogramming, and immune escape. Because these carcinogenic events can occur in any temporal sequence in vivo, molecular and genetic analyses cannot fully deconvolve the intermediate steps preceding the final tumor product. The mKit^{K641E} set of isogenically matched lines is thus an ideal model to better study oncogenic events in distinct biologically relevant stages. One integrative model is shown in Figure 9.

Transformation induced the most significant molecular changes among the various stages. Its attendant pathways underscore the heavy cellular expense required by heightened cell cycling and mitotic activity. Programs that serve metabolic demand can be observed at all levels, including DNA replication, protein translation, and lipid/cholesterol biosynthesis for membrane constituents. Although these biosynthetic pathways are most significant in the stage-wise comparison between PT (+Kit^{K641E}) and vector (control), they are also observed in supercluster I and are enriched in the subsequent lifecycle of the tumor. Thus Kit^{K641E} and

perhaps other oncogenes may permanently reconfigure the cell cycle engine independent of the host. Notably, these programmatic findings are consistent with the replication stress described for this model (Njauw et al, 2022).

Kit^{K641E} tumorigenesis in an immunodeficient host (ie, N1 cells) recapitulates many axonal and synaptic apparatuses used during neural development. Although speculative, Kit^{K641E} invasion into the immune-free host stroma may be regulated by the same developmental processes involved in neuronal and axonal migration. *Wnt5a*—a member of both the axon development and synaptic organization gene sets— is one of the most highly induced transcripts (N1 vs PT: log$_2$ fold change = +9.62, adjusted P = 1.82E-11) during this phase of initial tumor formation. The WNT pathway, including *WNT5A*, is well-known to positively regulate melanoma invasiveness (Da Forno et al, 2008; Webster et al, 2015; Weeraratna et al, 2002). Both *Sema3f* and *Plxnd1* levels significantly increased during tumorigenesis, along with *Sema3a*, *Sema3c*, *Sema4c*, *Sema4f*, *Sema6d*, and *Sema7a*. Although SEMA3−PLXND1 signaling is known to regulate axon guidance and pruning, this pairing is also involved in cardiovascular patterning and angiogenesis (Gay et al, 2011), which is strongly correlated with tumorigenesis (angiogenesis, GO:0001525, q = 4.45E-05). In addition, axon guidance genes have been implicated in pancreatic cancer (Biankin et al, 2012) and uveal melanomas (Field et al, 2019), whereas the semaphorin molecules are now known to play critical roles in both axon guidance and tumor regulation (Ahammad, 2020). In the cluster analysis, many axon/synapse molecules were initially suppressed during transformation but were followed by a strong rebound in expression during tumorigenesis. On the basis of the pathway analyses, this pattern could partly underpin the biological toggle between proliferation and invasion (Gao et al, 2005).

As shown in Figure 2b, immune engagement and tumor escalation in C57BL/6 mice were associated with fewer gene expression changes than the initial tumorigenic phase in NSG mice. This suggests that a major survival barrier in vivo was
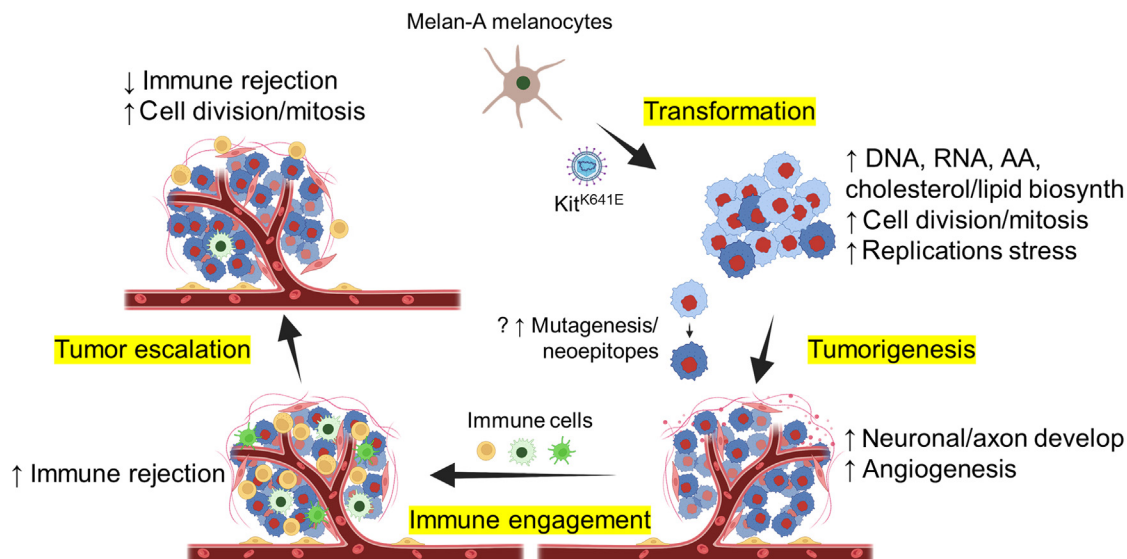

Figure 9. Model of mKit^{K641E} melanoma progression. Schematic representation of the progression of *KIT*-mutated melanoma tumors through the 4 major stages of tumor progression, with top enriched pathways labeled.

already breached in NSG mice. Moreover, the relationship between the immune system and Kit^K641E tumorigenesis is complex and biphasic. Initial allotransplantation of mKit^K641E cells leads to activation of immune rejection pathways (eg, graft vs host and allograft rejection). However, as tumor escalation proceeds, this rejection response attenuates (Figure 4a). One possibility is that progressive mutagenesis of the melan-A cells during transformation and tumorigenesis leads to a novel repertoire of neoantigens, which then triggers a robust immune rejection physiology upon first immune exposure. Serial transplantation of the mKit^K641E cells may cause subsequent immunoediting, sequence variant pruning, and a defervescence of inflammation. Alternatively, replication stress, which has been demonstrated in the mKit^K641E model (Njauw et al, 2022), may autonomously activate a proinflammatory response through the cGAS—STING (stimulator of interferon genes) pathway (reviewed in Ragu et al [2020]). Cells that accumulate cytoplasmic and nuclear double-strand and single-strand DNA due to replication stress can trigger an innate immune reaction, which could explain the enrichments for IFNβ and various viral infections (eg, measles, human papillomavirus) during tumorigenesis.

Both murine and human *KIT*-altered melanomas appear to activate mitochondrial/cellular respiration and lineage identity pathways; these 2 distinct physiologies could conceivably be linked. It has been reported that MITF induces the expression of PGC1α (*PPARGC1A*)—the master regulator of mitochondrial biogenesis—in a specific subset of human melanomas and their derived cell lines. Melanoma cells with high levels of PGC1α exhibit enhanced mitochondrial energy metabolism and increased capacity to detoxify ROS (Vazquez et al, 2013). More recently, Huang et al (2014) showed that SCF/Kit regulates mitochondrial function and energy homeostasis by modulating PGC1α expression. *Kit*-deficient mice exhibit decreased PGC1α expression, reduced mitochondrial biogenesis and energy expenditure, and progressive obesity (Huang et al, 2014). Ectopic overexpression of *Kitl* in the *Kit*-mutant mice attenuated the weight gain. Finally, mitochondrial dysfunction has been implicated in both Parkinson's and Huntington's diseases (Jodeiri Farshbaf and Ghaedi, 2017; Li et al, 2021), which could explain the substantial overrepresentation of these pathways in *KIT*-mutant tumors. It stands to reason that primordial neural specification and mitochondrial dysfunction may underpin elements of KIT-selective programming in melanomas.

There are several limitations to these studies. First, serializing Kit^K641E oncogenesis affords certain analytical conveniences, although human cancer biology evolves concurrently and encompasses heterogeneity. For instance, mutagenesis and immune stimulation may occur in concert with other cells undergoing immune evasion. Furthermore, as human cells transform, ongoing immune editing may simultaneously prune nascent tumor cells. Nevertheless, our study provides a framework for understanding the molecular underpinnings of the observed cancer phenotypes. Second, although we explore commonalities between the mouse Kit^K641E model and human KIT-altered tumors specifically, many of the energetic and replicative pathways may be shared among different oncogenic triggers. These constitute ongoing studies using other allograft models generated using the same melan-A parent cell and the same tumor development protocol. Third, the Kit p.K641E variant represents a single oncogenic allele, whereas multiple activating variants are known to exist in human melanoma (Pham et al, 2020). We aggregated all human KIT alterations into 1 bucket to gain analytical power for comparative purposes. Once expanded databases become available for study, variant-specific biology among human *KIT*-mutant tumors will become more feasible. Fourth, although these studies aim to explicate molecular programs accompanying each carcinogenic stage, genetic events that drive stage-wise progression have not been thoroughly studied. Whole-exome sequencing of the various mKit^K641E lines is underway to complement our analysis. Finally, RNA expression allows for broad profiling of numerous genes but is not a surrogate for protein levels. Confirmatory studies still need to be performed to explicate the protein—protein interactome and networks that underlie the oncogenic physiology.

Cancer cells negotiate several critical milestones to evolve into a sustainable entity. These physiological events include the ignition of the replicative and biosynthetic engine, host habitation, and immune evasion. This study provides one framework to understand the dynamic programming required at various stages for Kit oncogenesis and documents a possible connection between pigment lineage and metabolism that may selectively underpin *KIT*-mutant melanomas.

MATERIALS AND METHODS
Cell lines
Derivation and characterization of the mKit^K641E lines can be found in Njauw et al (2022); cells were made available by the authors. The general scheme is shown in Figure 1. The tumors and cells were collected under a protocol approved by the Massachusetts General Hospital Institutional Animal Care and Use Committee (number 2014N000314).

RNA extraction and raw files
Total RNA was isolated using Trizol followed by Qiagen RNeasy Plus Mini Kit (Qiagen). RNA quality was assessed by Fragment Analyzer High Sensitivity RNA Assay (Agilent Technologies) and quantified with Qubit 2.0 RNA HS assay (Thermo Fisher Scientific). Paramagnetic beads coupled with oligo d(T)25 were combined with total RNA to isolate poly(A)+ transcripts on the basis of NEBNext Poly(A) mRNA Magnetic Isolation Module manual (New England BioLabs). Before first strand synthesis, samples were randomly primed (5′ d [N6] 3′ [N = A, C, G, T]) and fragmented on the basis of the manufacturer's instructions. The first strand was synthesized with the Protoscript II Reverse Transcriptase for 30 minutes at 42 °C. All remaining steps for library construction were performed according to the NEBNext Ultra II Non-Directional RNA Library Prep Kit for Illumina (New England BioLabs). The final library quantity and quality were assessed by Qubit 2.0 (Thermo Fisher Scientific) and the TapeStation HSD1000 ScreenTape (Agilent Technologies), respectively. The library size was about 400 bp with an insert size of about 250 bp. Illumina 8-nt dual indices were used. Equimolar pooling of libraries was performed on the basis of quality control values and sequenced on an Illumina NovaSeq 6000 (Illumina) with a read length configuration of 150 PE for 40 M PE reads per sample (20 M in each direction).

The reference genome was Genome Reference Consortium Mouse Build 38 (Mm10). FastQC (version 0.11.8) was applied to check the quality of raw reads. Trimmomatic (version 0.38) was applied to cut adaptors and trim low-quality bases with the default settings. STAR Aligner, version 2.7.1a, was used to align the reads, and Picard tools (version 2.20.4) were applied to mark duplicates of mapping. StringTie, version 2.0.4, was used to assemble the RNA-sequencing alignments into potential transcripts. The featureCounts (version 1.6.0)/HTSeq was used to count mapped reads for genomic features such as genes, exons, promoters, gene bodies, genomic bins, and chromosomal locations. DESeq2 (version 1.14.1) was used to do the differential analysis. Chipseeker package annotated the peaks (RNA sequencing report from Admera Health, LLC).

Stage-wise analysis

Differential gene expression analysis was done using DESeq2 (version 1.40.1, https://bioconductor.org/packages/release/bioc/html/DESeq2.html) R package. Count data produced from HTseq-count were imported to DESeq2 pipeline by the function DESeqDataSetFromHTSeqCount. Prefiltering was conducted to ensure that only rows with at least 10 reads were kept. The data were then analyzed by the DESeq function, which uses the Wald test to identify differentially expressed genes. We used the default false discovery rate of 0.1 to indicate significance. Log$_2$ fold change estimates were shrunken using the function lfcShrink with a Normal prior.

Principal component analysis

We transformed the count data to log2 scale by the rlog function from the DESeq2 package to minimize differences between samples for rows with small counts. Principal components analysis was then performed with the prcomp function from R stats package. The first and second principal components were then plotted with ggplot2 package.

Cluster analysis

The count data were first analyzed by DESeq function, with likelihood ratio test as the hypothesis testing method. The extracted results were then filtered using a cutoff of 0.05 for the adjusted *P*-values. With the degPatterns function from the DEGreport package, clusters of genes that exhibited similar expression patterns across sample groups were identified and plotted.

Superclusters were generated on the basis of the mean expression levels of all genes within each cluster × stage; hierarchical clustering was then performed using Past4.03 (https://folk.universitetetioslo.no/ohammer/past) with Ward's method in Euclidean space.

Pathway analysis

Pathway enrichment analysis was done to obtain a complete picture of gene expression changes between the different stages of tumor progression. All run dates are shown in their respective tables. We used gene sets comparing the following stages: PT with vector, N1 with PT, C1 with N1, C3 with C1, and C3 with vector. We performed gene set analysis using both ORA and Gene Set Enrichment Analysis using an online functional enrichment gene set analysis tool, Webgestalt (https://www.webgestalt.org).

We first ran ORA on all stage comparisons, with the list of genes in each stage-specific comparison filtered by a log$_2$ fold change > 1 and adjusted *P* < .05. The parameters used were organism of interest: mmusculus; method of interest: overrepresentation analysis; functional database: geneontology and pathway; functional database name: biological_Process_noRedundant, cellular_component_noRedundant, molecular_Function_noRedundant for gene ontology setting and KEGG, Panther, Reactome, and Wikipathway for pathway setting; gene identification type: genesymbol; gene reference set: Genome; minimum number of genes for a category: 5; maximum number of genes for a category: 10,000; multiple test adjustment: Benjamini−Hochberg; significance level: false discovery rate = 0.05; number of categories expected from set cover: 10; number of categories visualized in the report: 100; and color in Directed Acyclic Graph: continuous.

We then used Gene Set Enrichment Analysis to perform a ranked gene set analysis on the genes in each stage-specific comparison using all genes in the gene set with an available gene name, with genes ranked from largest to smallest log$_2$ fold change. The parameters used were organism of interest: mmusculus; method of interest: Gene Set Enrichment Analysis; functional database: pathway; functional database name: KEGG, Panther, Reactome, and Wikipathway; gene identification type: genesymbol; gene reference set: genome; minimum number of genes for a category: 5; maximum number of genes for a category: 10,000; multiple test adjustment: Benjamini−Hochberg; significance level: false discovery rate = 0.05; number of permutations: 1000; number of categories with leading-edge genes: 20; collapse method: mean; number of categories visualized in the report: 100; and color in Directed Acyclic Graph: continuous.

Human melanoma analysis

The deidentified publicly available The Cancer Genome Atlas SKCM PanCancer dataset (complete samples; n = 363) (https://www.cbioportal.org/) was used for comparative human *KIT* analysis. The list of KIT-altered (h*KIT*^alt) and wild-type (h*KIT*^wt) human melanomas are listed in Supplementary Table S8. Differential gene expression between h*KIT*^alt and h*KIT*^wt was performed using the built-in module (comparison/survival:mRNA) with mRNA Expression, RSEM (RNA-Seq by Expectation-Maximization) (Batch normalized from Illumina HiSeq_RNASeqV2), corresponding to the rsem.genes.normalized_results file from The Cancer Genome Atlas.

ORCIDs

Emily Everdell: http://orcid.org/0000-0001-5740-7205
Zhenyu Ji: http://orcid.org/0000-0002-3353-6376
Ching-Ni Njauw: http://orcid.org/0000-0003-4543-3769
Hensin Tsao: http://orcid.org/0000-0002-2204-2071

CONFLICT OF INTEREST

The authors state no conflict of interest.

AUTHOR CONTRIBUTIONS

Conceptualization: EE, ZJ, CNN, HT; Investigation, Methodology: ZJ, CNN; Data Curation: EE, ZJ, CNN; Formal Analysis: EE, ZJ; Funding Acquisition: HT; Supervision: HT; Validation, Visualization: EE, ZJ, CNN, HT; Writing: EE, ZJ, CNN, HT

SUPPLEMENTARY MATERIAL

Supplementary material is linked to the online version of the paper at www.jidonline.org, and at https://doi.org/10.1016/j.xjidi.2024.100266.

REFERENCES

Ahammad I. A comprehensive review of tumor proliferative and suppressive role of semaphorins and therapeutic approaches. Biophys Rev 2020;12:1233−47.

Beadling C, Jacobson-Dunlop E, Hodi FS, Le C, Warrick A, Patterson J, et al. KIT gene mutations and copy number in melanoma subtypes. Clin Cancer Res 2008;14:6821−8.

Biankin AV, Waddell N, Kassahn KS, Gingras MC, Muthuswamy LB, Johns AL, et al. Pancreatic cancer genomes reveal aberrations in axon guidance pathway genes. Nature 2012;491:399−405.

Bradford PT, Goldstein AM, McMaster ML, Tucker MA. Acral lentiginous melanoma: incidence and survival patterns in the United States, 1986−2005. Arch Dermatol 2009;145:427−34.

Chang AE, Karnell LH, Menck HR. The National Cancer Data Base report on cutaneous and noncutaneous melanoma: a summary of 84,836 cases from the past decade. The American College of Surgeons Commission on Cancer and the American Cancer Society. Cancer 1998;83:1664−78.

Curtin JA, Fridlyand J, Kageshita T, Patel HN, Busam KJ, Kutzner H, et al. Distinct sets of genetic alterations in melanoma. N Engl J Med 2005;353:2135−47.

Da Forno PD, Pringle JH, Hutchinson P, Osborn J, Huang Q, Potter L, et al. WNT5A expression increases during melanoma progression and correlates with outcome. Clin Cancer Res 2008;14:5825−32.

de Lima Vazquez V, Vicente AL, Carloni A, Berardinelli G, Soares P, Scapulatempo C, et al. Molecular profiling, including tert promoter mutations, of acral lentiginous melanomas. Melanoma Res 2016;26:93−9.

Field MG, Kuznetsov JN, Bussies PL, Cai LZ, Alawa KA, Decatur CL, et al. BAP1 loss is associated with DNA methylomic repatterning in highly aggressive Class 2 uveal melanomas. Clin Cancer Res 2019;25:5663−73.

Gao CF, Xie Q, Su YL, Koeman J, Khoo SK, Gustafson M, et al. Proliferation and invasion: plasticity in tumor cells. Proc Natl Acad Sci USA 2005;102:10528−33.

Gay CM, Zygmunt T, Torres-Vázquez J. Diverse functions for the semaphorin receptor PlexinD1 in development and disease. Dev Biol 2011;349:1−19.

Hanahan D, Weinberg RA. Hallmarks of cancer: the next generation. Cell 2011;144:646−74.

Huang Z, Ruan HB, Xian L, Chen W, Jiang S, Song A, et al. The stem cell factor/Kit signalling pathway regulates mitochondrial function and energy expenditure. Nat Commun 2014;5:4282.

Jodeiri Farshbaf M, Ghaedi K. Huntington's disease and mitochondria. Neurotox Res 2017;32:518−29.

Kong Y, Si L, Zhu Y, Xu X, Corless CL, Flaherty KT, et al. Large-scale analysis of KIT aberrations in Chinese patients with melanoma. Clin Cancer Res 2011;17:1684−91.

Li JL, Lin TY, Chen PL, Guo TN, Huang SY, Chen CH, et al. Mitochondrial function and Parkinson's disease: from the perspective of the electron transport chain. Front Mol Neurosci 2021;14:797833.

Meng D, Carvajal RD. KIT as an oncogenic driver in melanoma: an update on clinical development. Am J Clin Dermatol 2019;20:315−23.

Mihajlovic M, Vlajkovic S, Jovanovic P, Stefanovic V. Primary mucosal melanomas: a comprehensive review. Int J Clin Exp Pathol 2012;5:739−53.

Newell F, Kong Y, Wilmott JS, Johansson PA, Ferguson PM, Cui C, et al. Whole-genome landscape of mucosal melanoma reveals diverse drivers and therapeutic targets. Nat Commun 2019;10:3163.

Njauw CN, Ji Z, Pham DM, Simoneau A, Kumar R, Flaherty KT, et al. Oncogenic KIT induces replication stress and confers cell cycle checkpoint vulnerability in melanoma. J Invest Dermatol 2022;142:1413−24.e6.

Pham DDM, Guhan S, Tsao H. KIT and melanoma: biological insights and clinical implications. Yonsei Med J 2020;61:562−71.

Ragu S, Matos-Rodrigues G, Lopez BS. Replication stress, DNA damage, inflammatory cytokines and innate immune response. Genes (Basel) 2020;11:409.

Reintgen DS, McCarty KM Jr, Cox E, Seigler HF. Malignant melanoma in black American and white American populations. A comparative review. JAMA 1982;248:1856−9.

Rouhani P, Hu S, Kirsner RS. Melanoma in Hispanic and black Americans. Cancer Control 2008;15:248−53.

Rubin BP, Antonescu CR, Scott-Browne JP, Comstock ML, Gu Y, Tanas MR, et al. A knock-in mouse model of gastrointestinal stromal tumor harboring kit K641E. Cancer Res 2005;65:6631−9.

Shaikh WR, Dusza SW, Weinstock MA, Oliveria SA, Geller AC, Halpern AC. Melanoma thickness and survival trends in the United States, 1989 to 2009. J Natl Cancer Inst 2015;108:djv294.

Shibahara S, Takeda K, Yasumoto K, Udono T, Watanabe K, Saito H, et al. Microphthalmia-associated transcription factor (MITF): multiplicity in structure, function, and regulation. J Investig Dermatol Symp Proc 2001;6:99−104.

Sturm G, Finotello F, Petitprez F, Zhang JD, Baumbach J, Fridman WH, et al. Comprehensive evaluation of transcriptome-based cell-type quantification methods for immuno-oncology. Bioinformatics 2019;35:i436−45.

Todd JR, Becker TM, Kefford RF, Rizos H. Secondary c-Kit mutations confer acquired resistance to RTK inhibitors in c-Kit mutant melanoma cells. Pigment Cell Melanoma Res 2013;26:518−26.

Vazquez F, Lim JH, Chim H, Bhalla K, Girnun G, Pierce K, et al. PGC1alpha expression defines a subset of human melanoma tumors with increased mitochondrial capacity and resistance to oxidative stress. Cancer Cell 2013;23:287−301.

Webster MR, Xu M, Kinzler KA, Kaur A, Appleton J, O'Connell MP, et al. Wnt5A promotes an adaptive, senescent-like stress response, while continuing to drive invasion in melanoma cells. Pigment Cell Melanoma Res 2015;28:184−95.

Weeraratna AT, Jiang Y, Hostetter G, Rosenblatt K, Duray P, Bittner M, et al. Wnt5a signaling directly affects cell motility and invasion of metastatic melanoma. Cancer Cell 2002;1:279−88.

Wu XC, Eide MJ, King J, Saraiya M, Huang Y, Wiggins C, et al. Racial and ethnic variations in incidence and survival of cutaneous melanoma in the United States, 1999−2006. J Am Acad Dermatol 2011;65:S26−37.

Zebary A, Omholt K, Vassilaki I, Höiom V, Lindén D, Viberg L, et al. KIT, NRAS, BRAF and PTEN mutations in a sample of Swedish patients with acral lentiginous melanoma. J Dermatol Sci 2013;72:284−9.

Zell JA, Cinar P, Mobasher M, Ziogas A, Meyskens FL Jr, Anton-Culver H. Survival for patients with invasive cutaneous melanoma among ethnic groups: the effects of socioeconomic status and treatment. J Clin Oncol 2008;26:66−75.

Zhan Y, Guo J, Yang W, Goncalves C, Rzymski T, Dreas A, et al. MNK1/2 inhibition limits oncogenicity and metastasis of KIT-mutant melanoma. J Clin Invest 2017;127:4179−92.